Classification of peacock feather reflectance using principal component analysis similarity factors from multispectral imaging data

José M. Medina,[1,*] José A. Díaz,[1] and Pete Vukusic[2]

[1]*Universidad de Granada, Facultad de Ciencias, Departamento de Óptica, Edificio Mecenas, Granada 18071, Spain*
[2]*School of Physics, University of Exeter, EX4 4QL, UK*
[*]*jmedinaru@cofis.es*

Abstract: Iridescent structural colors in biology exhibit sophisticated spatially-varying reflectance properties that depend on both the illumination and viewing angles. The classification of such spectral and spatial information in iridescent structurally colored surfaces is important to elucidate the functional role of irregularity and to improve understanding of color pattern formation at different length scales. In this study, we propose a non-invasive method for the spectral classification of spatial reflectance patterns at the micron scale based on the multispectral imaging technique and the principal component analysis similarity factor (PCASF). We demonstrate the effectiveness of this approach and its component methods by detailing its use in the study of the angle-dependent reflectance properties of *Pavo cristatus* (the common peacock) feathers, a species of peafowl very well known to exhibit bright and saturated iridescent colors. We show that multispectral reflectance imaging and PCASF approaches can be used as effective tools for spectral recognition of iridescent patterns in the visible spectrum and provide meaningful information for spectral classification of the irregularity of the microstructure in iridescent plumage.

OCIS codes: (170.1420) Biology; (330.1690) Color; (350.4238) Nanophotonics and photonic crystals; (310.6188) Spectral properties; (110.4234) Multispectral and hyperspectral imaging; (100.5010) Pattern recognition.

References and links

1. S. Kinoshita, S. Yoshioka, and J. Miyazaki, "Physics of structural colors," Rep. Prog. Phys. **71**(7), 076401 (2008).
2. R. O. Prum, R. H. Torres, S. Williamson, and J. Dyck, "Coherent light scattering by blue feather barbs," Nature **396**(6706), 28–29 (1998).
3. R. O. Prum, R. Torres, S. Williamson, and J. Dyck, "Two-dimensional Fourier analysis of the spongy medullary keratin of structurally coloured feather barbs," Proc. R. Soc. Lond. B Biol. Sci. **266**(1414), 13–22 (1999).
4. R. O. Prum and R. H. Torres, "A Fourier tool for the analysis of coherent light scattering by bio-optical nanostructures," Integr. Comp. Biol. **43**(4), 591–602 (2003).
5. H. Durrer, "Schillerfarben beim Pfau (*Pavo cristatus* L.)," Verh. Naturf. Ges. Basel **73**, 204–224 (1962).
6. C. W. Mason, "Structural colors in feathers II," J. Phys. Chem. **27**(5), 401–448 (1922).
7. J. Zi, X. Yu, Y. Li, X. Hu, C. Xu, X. Wang, X. Liu, and R. Fu, "Coloration strategies in peacock feathers," Proc. Natl. Acad. Sci. U.S.A. **100**(22), 12576–12578 (2003).
8. Y. Li, Z. Lu, H. Yin, X. Yu, X. Liu, and J. Zi, "Structural origin of the brown color of barbules in male peacock tail feathers," Phys. Rev. E Stat. Nonlin. Soft Matter Phys. **72**(1), 010902 (2005).
9. S. Yoshioka and S. Kinoshita, "Effect of macroscopic structure in iridescent color of the peacock feathers," Forma **17**, 169–181 (2002).
10. S. C. Burgess, A. King, and R. Hyde, "An analysis of optimal structural features in the peacock tail feather," Opt. Lasers Eng. **38**(4-6), 329–334 (2006).
11. V. E. Johansen, "Optical role of randomness for structured surfaces," Appl. Opt. **53**(11), 2405–2415 (2014).
12. A. Loyau, D. Gomez, B. Moureau, M. Théry, N. S. Hart, M. S. Jalme, A. T. D. Bennett, and G. Sorci, "Iridescent structurally based coloration of eyespots correlates with mating success in the peacock," Behav. Ecol. **18**(6), 1123–1131 (2007).
13. P. Vukusic and D. G. Stavenga, "Physical methods for investigating structural colours in biological systems," J. R. Soc. Interface **6**(Suppl 2), S133–S148 (2009).

14. D. Osorio and A. D. Ham, "Spectral reflectance and directional properties of structural coloration in bird plumage," J. Exp. Biol. **205**(Pt 14), 2017–2027 (2002).
15. D. J. Brink and N. G. Berg, "Structural colours from the feathers of the bird Bostrychia hagedash," J. Phys. D Appl. Phys. **37**(5), 813–818 (2004).
16. H. Yin, L. Shi, J. Sha, Y. Li, Y. Qin, B. Dong, S. Meyer, X. Liu, L. Zhao, and J. Zi, "Iridescence in the neck feathers of domestic pigeons," Phys. Rev. E Stat. Nonlin. Soft Matter Phys. **74**(5), 051916 (2006).
17. M. C. Stoddard and R. O. Prum, "Evolution of avian plumage color in a tetrahedral color space: A phylogenetic analysis of new world buntings," Am. Nat. **171**(6), 755–776 (2008).
18. D. G. Stavenga, H. L. Leertouwer, N. J. Marshall, and D. Osorio, "Dramatic colour changes in a bird of paradise caused by uniquely structured breast feather barbules," Proc. Biol. Sci. **278**(1715), 2098–2104 (2011).
19. M. Meadows, N. Morehouse, R. Rutowski, J. Douglas, and K. McGraw, "Quantifying iridescent coloration in animals: a method for improving repeatability," Behav. Ecol. Sociobiol. **65**(6), 1317–1327 (2011).
20. M. C. Stoddard and R. O. Prum, "How colorful are birds? Evolution of the avian plumage color gamut," Behav. Ecol. **22**(5), 1042–1052 (2011).
21. D. G. Stavenga, H. L. Leertouwer, P. Pirih, and M. F. Wehling, "Imaging scatterometry of butterfly wing scales," Opt. Express **17**(1), 193–202 (2009).
22. M. H. Kim, H. Rushmeier, J. Dorsey, T. A. Harvey, R. O. Prum, D. S. Kittle, and D. J. Brady, "3D Imaging spectroscopy for measuring hyperspectral patterns on solid objects," ACM Trans. Graph. **31**, 1–11 (2012).
23. T. A. Harvey, K. S. Bostwick, and S. Marschner, "Measuring spatially- and directionally-varying light scattering from biological material," J. Vis. Exp. **75**(75), e50254 (2013).
24. T. A. Harvey, K. S. Bostwick, and S. Marschner, "Directional reflectance and milli-scale feather morphology of the African Emerald Cuckoo, Chrysococcyx cupreus," J. R. Soc. Interface **10**(86), 20130391 (2013).
25. M. Brydegaard, P. Samuelsson, M. W. Kudenov, and S. Svanberg, "On the exploitation of mid-infrared iridescence of plumage for remote classification of nocturnal migrating birds," Appl. Spectrosc. **67**(5), 477–490 (2013).
26. J. Craven-Jones, M. W. Kudenov, M. G. Stapelbroek, and E. L. Dereniak, "Infrared hyperspectral imaging polarimeter using birefringent prisms," Appl. Opt. **50**(8), 1170–1185 (2011).
27. M. W. Kudenov and E. L. Dereniak, "Compact snapshot real-time imaging spectrometer," Proc. SPIE **8186**, 81860W, 81860W-12 (2011).
28. M. W. Kudenov, M. J. Escuti, E. L. Dereniak, and K. Oka, "White-light channeled imaging polarimeter using broadband polarization gratings," Appl. Opt. **50**(15), 2283–2293 (2011).
29. N. Gat, "Imaging spectroscopy using tunable filters: a review," Proc. SPIE **4056**, 50–64 (2000).
30. H. F. Grahn and P. Geladi, *Techniques and Applications of Hyperspectral Image Analysis* (John Wiley & Sons, 2007).
31. A. F. H. Goetz, G. Vane, J. E. Solomon, and B. N. Rock, "Imaging spectrometry for Earth remote sensing," Science **228**(4704), 1147–1153 (1985).
32. M. Ottavian, P. Facco, L. Fasolato, and M. Barolo, "Multispectral data classification using similarity factors," Chemometr. Intell. Lab. **118**, 13–23 (2012).
33. A. Singhal and D. E. Seborg, "Matching patterns from historical data using PCA and distance similarity factors," in *Proceedings of the American Control Conference,* (IEEE, 2001), pp. 1759–1764.
34. W. J. Krzanowski, "Between groups comparison of principal components," JASA **74**(367), 703–707 (1979).
35. M. C. Johannesmeyer, A. Singhal, and D. E. Seborg, "Pattern matching in historical data," AIChE J. **48**(9), 2022–2038 (2002).
36. C. C. Chiao, T. W. Cronin, and D. Osorio, "Color signals in natural scenes: characteristics of reflectance spectra and effects of natural illuminants," J. Opt. Soc. Am. A **17**(2), 218–224 (2000).
37. P. Bajorski, *Statistics for Imaging, Optics, and Photonics* (John Wiley & Sons, 2012).
38. J. M. Lopez-Alonso and J. Alda, "Characterization of scenarios for multiband and hyperspectral imagers," Proc. SPIE **5439**, 140–149 (2004).
39. J. M. Lopez-Alonso and J. Alda, "Characterization of hyperspectral imagers and scenes: background and equipment artifacts," Proc. SPIE **5612**, 265–274 (2004).
40. D. Y. Tzeng and R. S. Berns, "A review of principal component analysis and its applications to color technology," Color Res. Appl. **30**(2), 84–98 (2005).
41. J. M. Medina, "Linear basis for metallic and iridescent colors," Appl. Opt. **47**(30), 5644–5653 (2008).
42. I. T. Jolliffe, *Principal Component Analysis,* Second ed., Springer Series in Statistics (Springer-Verlag, 2002).
43. A. Kelber, M. Vorobyev, and D. Osorio, "Animal colour vision - behavioural tests and physiological concepts," Biol. Rev. Camb. Philos. Soc. **78**(1), 81–118 (2003).
44. G. Wyszecki and W. S. Stiles, *Color Science: Concepts and Methods, Quantitative Data and Formulae* (John Wiley & Sons, 1982).
45. I. M. Weiss and H. O. K. Kirchner, "The peacock's train (*Pavo cristatus* and *Pavo cristatus* mut. alba) I. structure, mechanics, and chemistry of the tail feather coverts," J. Exp. Zool. A Ecol. Genet. Physiol. **313A**, 690–703 (2010).
46. S. Pabisch, S. Puchegger, H. O. K. Kirchner, I. M. Weiss, and H. Peterlik, "Keratin homogeneity in the tail feathers of *Pavo cristatus* and *Pavo cristatus* mut. alba," J. Struct. Biol. **172**(3), 270–275 (2010).
47. P. Simonis, M. Rattal, M. Oualim, A. Mouhse, and J.-P. Vigneron, "Radiative contribution to thermal conductance in animal furs and other woolly insulators," Opt. Express **22**(2), 1940–1951 (2014).
48. M. Mishra, "Transformation of colourful pattern of eyespot in peacock wing," Curr. Sci. **107**, 186–188 (2014).
49. B. Gralak, G. Tayeb, and S. Enoch, "Morpho butterflies wings color modeled with lamellar grating theory," Opt. Express **9**(11), 567–578 (2001).

50. A. Ngan, F. Durand, and W. Matusik, "Experimental analysis of BRDF models," in *Proceedings of the Sixteenth Eurographics Conference on Rendering Techniques,* (Eurographics Association, 2005), pp. 117–126.
51. R. Shimada and Y. Kawaguchi, "Spectral BRDF creation for structural colors," in *Proceedings of the ACM SIGGRAPH 2005,* (ACM Press, 2005), p. 48.
52. R. Shimada and Y. Kawaguchi, "BRDF estimation system for structural colors," in *Proceedings of the 2005 International Conference on Augmented Tele-Existence,* (ACM Press, 2005), pp. 16–21.
53. Y. Sun, "Rendering biological iridescences with RGB-based renderers," ACM Trans. Graph. **25**(1), 100–129 (2006).
54. H. Li, S.-C. Foo, K. E. Torrance, and S. H. Westin, "Automated three-axis gonioreflectometer for computer graphics applications," Opt. Eng. **45**, 043605 (2006).
55. D. B. Kim, M. K. Seo, K. Y. Kim, and K. H. Lee, "Acquisition and representation of pearlescent paints using an image-based goniospectrophotometer," Opt. Eng. **49**(4), 043604 (2010).
56. N. Okada, D. Zhu, D. Cai, J. Cole, M. Kambe, and S. Kinoshita, "Rendering Morpho butterflies based on high accuracy nano-optical simulation," J. Opt. **42**(1), 25–36 (2013).
57. F.- Wu and C.- Zheng, "Microfacet-based interference simulation for multilayer films," Graph. Models **78**, 26–35 (2015).
58. J. M. Medina, J. A. Díaz, E. Valero, J. L. Nieves, and P. Vukusic, "Detailed experimental characterization of reflectance spectra of *Sasakia charonda* butterfly using multispectral optical imaging," Opt. Eng. **53**(3), 033111 (2014).
59. M. Anderson, R. Motta, S. Chandrasekar, and M. Stokes, "Proposal for a standard default color space for the Internet - sRGB," in *Proceedings of the IS&T/SID Fourth Color Imaging Conference: Color Science, Systems and Applications,* (The Society for Imaging Science and Technology, 1996), pp. 238–245.
60. K. R. Millington, "Diffuse reflectance spectroscopy of fibrous proteins," Amino Acids **43**(3), 1277–1285 (2012).

1. Introduction

The brilliant iridescent color appearances of many avian feathers are produced by complex optical phenomena. They principally arise from coherent light scattering from self-assembled quasi-ordered structures that have a spatially periodic variation in refractive index. This can lead to iridescent colors [1–4]. A canonical example is the well-known iridescent effects of male peacock tail feathers [Fig. 1(a)] [5, 6].Within the cortex of these feathers' barbules, melanin rods are arranged to create two-dimensional (2D) photonic crystal-like structures at the sub-micron scale [Fig. 1(b)] [7–9]. Polarization effects from the photonic structure are not discernable and do not strongly influence the structural color appearance of feather barbules [7, 8]. The spatial organization of barbules is complex: it produces the intricate iridescent patterns of reflectance at the macro-scale which ultimately give rise to the visual effects that contribute to the bird's appearance [1, 6, 9, 10]. A certain extent of spatial disorder is crucial for achieving this appearance. An irregular spatial arrangement of barbules appears to smooth the angle-dependence of reflectance giving rise to the feather's diffuse reflection over a wide angular range [1, 9, 11]. The colorful eyespots of peacock feathers are also considered a classical example in research on intra-specific animal communication (i.e. relating to female mate choice) and do not exhibit reflectance maxima in the ultraviolet (UV) spectrum [12].

The measurement of the bi-directional reflectance distribution function (BRDF) in iridescent feathers is often simplified by fixing certain angles of illumination and detection [13]. Although several spectrophotometric methods have been implemented to examine the angular dependence of reflectance spectra over small feather patches [7–9, 12, 14–20], those studies that collect both spatial and spectral information simultaneously are rare. Stavenga *et al.* [18] have investigated light scattered patterns from a single boomerang-like barbule of the Lawes' parotia (*Parotia Lawesii*) using an imaging scatterometer based on an ellipsoidal mirror [13, 18, 21]. Kim *et al.* have used a snapshot-based hyperspectral acquisition system to compute three-dimensional (3D) spatial patterns and hyperspectral reflectance simultaneously, that extends from the near UV to the near infrared (IR) of the entire plumage of the Papuan Lorikeet (*Charmosyna papou goliathina*) and the Northern Rosella (*Platycercus venustus*) [22]. Harvey *et al.* have investigated the dependence between scattered light and orientation of feather barbs of the Purple Glossy Starling (*Lamprotornis purpureus*) and the African Emerald Cuckoo (*Chrysococcyx cupreus*) using a imaging scatterometer based on a spherical gantry configuration and an RGB camera [23, 24]. Brydegaard *et al.* have investigated the existence of iridescent effects in the mid-IR region of many avian species for remote classification at long distances [25]. They have concluded that these IR

iridescent features have a structural origin at the micrometer level. These authors have performed hyperspectral reflectance polarization imaging [26–28] of the Mallard (*Anas platyrhynchos*) demonstrating that IR iridescence persists in the entire bird [25].

In this study, we present details of a spectral classification method of reflectance patterns in the visible spectrum comprising the collection of series of multispectral images of peacock feathers, using a spatial resolution of a few microns, as a function of the illumination angle. Investigation of these reflectance patterns at the micrometer level has a direct link with the roughness of the microstructure and the spatial configuration of barbs and barbules [1, 9]. The peacock plumage is chosen to investigate if the emerging reflection patterns from quasi-periodic arrangement of structurally colored barbules can be classified among different categories of interest from the spectral perspective. For this purpose we have performed multispectral reflectance imaging on three representative peacock feather samples that exhibit different stages of feather development. This is also important in animal biometrics to examine the effects of weak microstructural disorder on iridescent colors across members of the same species. Multispectral imaging methods result from the combination of digital image analysis of an imaged scene and subsequent spectroscopic analysis pixel-by-pixel [29–31]. Multispectral imaging offers an important advantage for analysis of the micro-appearance of feathers by providing spectral data with high spatial resolution. Standard single-point spectrophotometric methods are limited because spatial details are often diluted within the illuminated area [13]. Multispectral imaging methods, however, enable the extraction of the spectral reflectance function at each pixel of the imaged scene [29, 30].
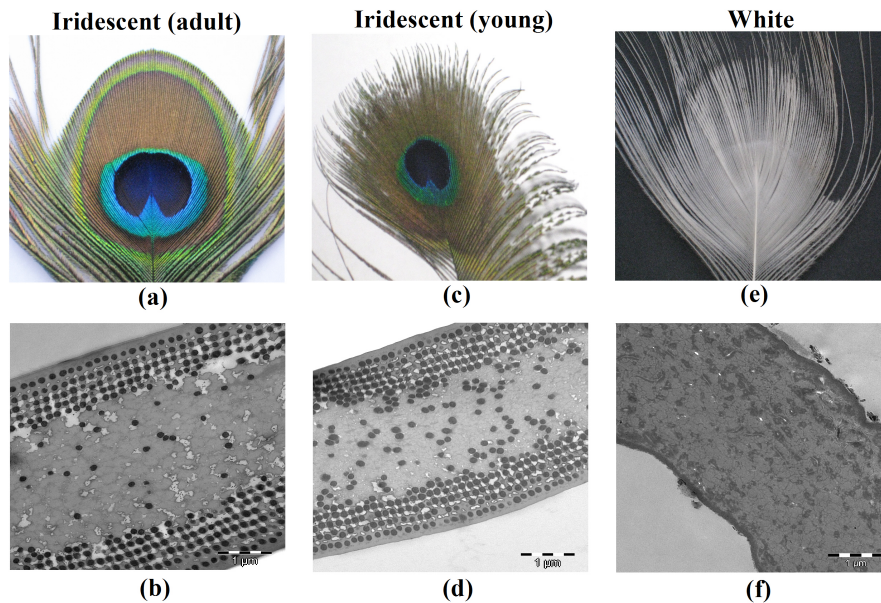

Fig. 1. Structural characterization of peacock tail feathers. Color photographs. Panels (a-c-e) show the eye region of an adult peacock feather (*P. cristatus*), a young peacock feather (*P. cristatus*), and a white peacock feather (*P. cristatus* mut. alba), respectively. Transmission electron micrographs (TEM). Panels (b-d-f) show TEM images of the transverse cross section of a brown barbule (adult *P. cristatus*), a brown barbule (young *P. cristatus*), and a white barbule (*P. cristatus* mut. alba) in the eyespot, respectively. Scale bars (b-d-f) 1 μm.

The principal components analysis similarity factor (PCASF) has previously been used for approach methodologies serving pattern recognition [32–34]. It is a PCA-based approach that is a useful technique for pattern matching which quantifies the similarity between two data sets in many industrial applications [32, 33, 35]. Principal component analysis (PCA) itself is an effective statistical method that has been widely used in multivariate image analysis for dimensionality reduction, data compression, classification, visualization, noise reduction, etc

[30, 32, 36–39]. In color science, PCA is also widely applied to uncover the spectral bands of colorants. PCA decomposes reflectance spectra into a linear combination of few uncorrelated basis functions or eigenvectors over a large number of reflectance data sets [32, 36, 37, 40, 41]. The first eigenvectors explain most of the variance within the data set [30, 37, 40, 42]. PCASF quantifies the similarity between the principal component subspaces that contain the most significant eigenvectors by using a single number. PCASF ranges from zero (no similarity) to one (similar samples) [32–35]. PCASF thereby enables comparison of the reflectance patterns created by arrays of feather barbs at different spatial locations, feather orientation, and illumination angles. Two different metrics were examined: the standard PCASF and a weighted PCASF (WPCASF). In the standard PCASF the eigenvectors are equally weighted, while in the WPCASF each eigenvector is weighted by the square root of its associated eigenvalue. WPCAF provides a measure of similarity using feature eigenvectors that explain a significant amount of variance [32, 35].

Classification of the reflectance properties of iridescent plumage overcomes current limitations of colorimetric methods [12, 17, 20, 43]. For example, classification of reflectance spectra does not depend on the illuminant spectra and receptor spectral sensitivities. Additionally, it avoids potentially misleading results from metamerism of pairs of color patterns [44]. In this study we illustrate PCASF by analyzing reflectance spectra collected from male peacock feathers (*Pavo cristatus*). We first describe PCASF between an iridescent peacock feather [Fig. 1(a)] and a white peacock feather (*Pavo cristatus* mut. alba) [Fig. 1(e)]. The white peacock belongs to the same species and displays non-iridescent effects. Its constituent feather barbules lack melanin rods [Fig. 1(f)] and its white color appearance is principally produced by broadband scattering in its keratin matrix [45–47]. We follow this by applying PCASF to the comparison of spatial reflectance patterns produced by feathers from an adult and a young peacock [Figs. 1(a) and 1(c)], where the young peacock feather is deemed to be in an intermediate state of growth [48]. In this sample the development of blue, green, brown and yellow barbules, as well as the spatial formation of the feather's eyespot region, are incomplete [Fig. 1(c)]. For instance, the brown barbules in the young peacock are thinner and the 2D photonic crystal structures in the cortex surface also reveal differences in the lattice structure [Fig. 1(d)]. The young and adult brown barbules have the same number of melanin layers (4 to 5). The lattice constant (rod spacing) along the direction parallel to the cortex, $a_\parallel$, is shorter in the young peacock. However, that in the perpendicular direction, $a_\perp$, is very similar to the adult peacock. The separation of the two melanin arrays nearest to the cortex, *d*, is slightly shorter in the young peacock [Figs. 1(b) and 1(d)]. These lattice values are similar to those previously reported for the *Pavo muticus*, a different species of peafowl [7, 8]. Table 1 summarizes the lattice constants of brown barbules in the young and adult peacock.

Table 1. Mean lattice constants $a_\parallel$, $a_\perp$ and the inter-distance between the two melanin arrays nearest to the cortex, *d*, of the 2D photonic structure of brown barbules in the young and adult peacock derived from TEM images [Figs. 1(d) and 1(b)]. The standard error of the mean (± 1SEM) is also shown.

Lattice constant	Young brown barbule	Adult brown barbule
	Mean (± 1 nm)	
$a_\parallel$	150 (2) nm	187 (3) nm
$a_\perp$	194 (3) nm	198 (4) nm
d	218 (4) nm	231 (5) nm

Further differences between TEM images in Figs. 1(d) and 1(b) can be found beneath the lattice structure at the center of brown barbules. There are more melanin rods in the young peacock that are randomly distributed. It has been suggested that these melanin granules offer increased absorption of transmitted light, reduce the extent of diffuse scattering, thereby making iridescent effects in these feathers more vivid [9].

2. Materials and methods

2.1 Structural analysis

Male peacock tail feathers were obtained from a farm in Málaga, Spain. Peacock feathers were characterized in Fig. 1 by using a digital color camera Canon PowerShot SD1000 and a transmission electron microscope (TEM) Carl Zeiss Libra 120 Plus EDX. TEM samples were prepared by fixing feather barbules in 2.5% glutaraldehyde in 0.1 M cacodylate buffer, pH 7.2 at 4 °C for 24 h, followed by rinsing in buffer for 1 h and 30 min at 4 °C. Barbules were then post-fixed in 1% aqueous OsO_4 in buffer at room temperature for 1 h followed by block staining in 2% aqueous uranyl acetate at room temperature for 2 h. Dehydratation was performed through a graded series of acetone ending with 100% acetone. Then, barbules were embedded in an epoxy resin (EMbed 812, EMS). Ultrathin microtome sample sections were stained with lead citrate.

2.2 Multispectral imaging acquisition system

Many theoretical and experimental approaches have been proposed for the calculation and measurement of the BRDF of anisotropic surface materials [9, 12–20, 22, 41, 49–57]. In computer graphics and rendering, the microscopic description of rough surfaces in structural colors is often modeled by using a collection of tiny facets or *microfacets* and physical-based models [49, 51–53, 56, 57]. Here we have used an experimental approach that comprises the measurement of components of the multispectral BRDF of a feather's surface microstructure using a calibrated multispectral camera in a simple goniometric stage. The multispectral imaging set up, procedure and spectral calibration are described in detail elsewhere [58], and it has been adapted to the study of peacock tail feathers. Figure 2 shows a schematic representation of the multispectral imaging acquisition system. Spectral reflectance information of peacock feathers varies with the illumination angle θ. Three different angular positions were established at the illumination angle θ of 15 °, 45 ° and 75 °. Collection of multispectral images was performed by tuning a liquid crystal tunable filter LCTF (Varispec VS-VIS2-10HC-35-SQ) from 410 nm to 700 nm in steps of 10 nm. The LCTF was attached in front of a lens (Navitar Zoom 7000 18: 108 mm) of a monochrome charge-couple device (CCD) camera (Retiga QImaging SVR1394). The illumination system uses a Hamamatsu L9588-04 150 W highly stable mercury xenon (Hg-Xe) lamp. Light is collected by an elliptical cold mirror and a Hamamatsu A10014-50-010 light guide with a condenser lens Hamamatsu E5147-06. At the distance of 20 cm perpendicular to the imaged surface, the lens uniformly irradiates an area of 40 mm diameter with a relative intensity 100%. This is equal to the intensity at 10 mm away from the output end of the light guide without the condenser lens. The condenser lens was mounted in a rotation stage Thorlabs RBB12. Peacock feather samples were mounted directly beneath a 50 mm diameter aperture [58]. The spectral reflectance factor at each pixel of the imaged surface was calculated by taking white- and dark-field measurements [29, 30, 36, 58]. The white-field correction indicates the intensity values of a calibration sample and was obtained by defocusing a white reflectance standard (Spectralon 99% Labsphere) [29, 30, 6, 58]. The dark-field correction denotes the intensity values of the dark current from the CCD sensor [29, 30, 36, 58] and was obtained with the light source off, without the sample holder, and preventing any residual light entering in the CCD camera [58]. The multispectral imaging system has a spatial resolution of 14.4 µm per pixel. Spectral calibration was done by using the Macbeth color checker chart [30, 37, 58].
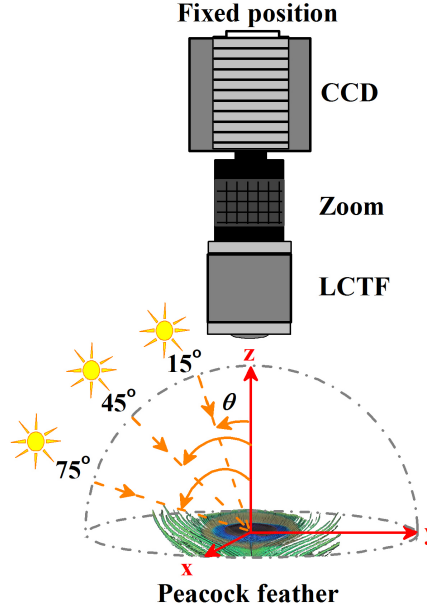
Fig. 2. Schematic representation of the multispectral imaging system. A liquid crystal tunable filter (LCTF) was placed in front of a zoom lens and attached to a monochrome charge-couple camera (CCD). The LCTF, zoom lens and CCD camera were in a fixed position and they were exactly aligned perpendicular to the sample. A light source module was connected to a light guide fiber. The fiber was mounted in a goniometric stage and was rotated at the illumination angle θ of 15 °, 45 ° and 75 °.

2.3 Principal component analysis of reflectance spectra

Reflectance spectra of each selected area were treated as a data matrix $\mathbf{R}$ of n rows of samples by 30 columns of wavelength intervals (at 10 nm resolution). $\mathbf{R}$ was centred around the corresponding mean reflectance factor $\bar{\mathbf{R}}$, $\mathbf{R} - \bar{\mathbf{R}}$. PCA decomposes $\mathbf{R}$ in the following matrix equation [30, 42]:

$$\mathbf{R} = \bar{\mathbf{R}} + \sum_{i=1}^{30} \boldsymbol{\alpha}_i \mathbf{S}_i \tag{1}$$

Where $\boldsymbol{\alpha}_i$ and $\mathbf{S}_i$ are the scores and the eigenvectors or loading vectors, respectively. Each eigenvector indicates the i-th principal component direction which reflectance spectra are distributed. Eigenvectors are often ranked in decreasing order of their associate eigenvalues β_i which correlates with decreasing order of variance accounted. In general, only the first k eigenvectors are taken in Eq. (1) using a stopping rule [30, 37, 42] that reduces the dimensionality of the original reflectance data set from 30 (as much dimensions as wavelength intervals) to k $(k < 30)$.

2.4 Principal component analysis similarity factors for reflectance spectra

The standard PCASF compares the relative angle $\phi_{i,j}$ between the eigenvectors of the two samples. The eigenvectors of the reference and test sample are arranged in the loading matrices $\mathbf{L}$ and $\mathbf{M}$, respectively, both with k principal components [32–34]:

$$PCASF = \sum_{i=1}^{k} \sum_{j=1}^{k} \cos^2 \phi_{i,j} = \frac{trace\left(\mathbf{M}^{\mathrm{T}} \mathbf{L} \mathbf{L}^{\mathrm{T}} \mathbf{M}\right)}{k} \tag{2}$$

The superscript T denotes the matrix transpose. A weighted PCASF or WPCASF weights each eigenvector by their associated eigenvalue to take into account the amount of variance explained by each principal component [32, 35]:

$$WPCASF = \frac{\sum_{i=1}^{k}\sum_{j=1}^{k}\beta_i^{L}\beta_j^{M}\cos^2\phi_{i,j}}{\sum_{i=1}^{k}\beta_i^{L}\beta_i^{M}} = \frac{trace\left(\mathbf{M}_{W}^{T}\mathbf{L}_{W}\mathbf{L}_{W}^{T}\mathbf{M}_{W}\right)}{\sum_{i=1}^{k}\beta_i^{L}\beta_i^{M}} \qquad (3)$$

$\mathbf{L}_{W} = \mathbf{L}\mathbf{\Lambda}_{L}$ and $\mathbf{M}_{W} = \mathbf{M}\mathbf{\Lambda}_{M}$ denote the weighted loading matrices. Subscripts and superscripts L and M denote the reference and test, respectively. In each case $\mathbf{\Lambda}_{L}$ and $\mathbf{\Lambda}_{M}$ are diagonal matrices that contain the square roots of the first k eigenvalues [32]. Therefore, each principal component direction is distinguished by its explained variance. This is relevant to the classification of spatial reflectance patterns because those principal components having low variance are of little importance in Eq. (3) and they are often associated with spatial and temporal noise from the multispectral imaging system [37–39, 58]. The number k of principal components is an important parameter in Eqs. (2) and (3). A widespread and accepted stopping rule in color science as well as in process monitoring comprises first selecting those eigenvectors that account for a certain percentage of total variance [32, 33, 35–37, 40, 41]. This stopping rule is adequate when the total spectral variability in the imaged scene is not very large [32, 36, 37, 58]. The number k was selected as the maximum value between the number of principal components of the reference and test sample that describe at least 95% of the total variance.

3. Results and discussion

3.1 Reconstruction in the sRGB color space

Figure 3 represents the entire selected imaging areas of size 841 x 841 pixels (146.6 mm^2) in the sRGB color space [8, 49, 58, 59]. The sRGB color space is intended for visualization in conventional color displays and the Internet [59]. Figures 3(a)-3(c) (left column), Figs. 3(d)-3(f) (central column) and Figs. 3(g)-3(i) (right column) correspond to the white, adult iridescent and young iridescent peacock feathers at the illumination angle θ of 15 °, 45 ° and 75 °, respectively. This gives a total of 9 different spatial color maps grouped in a matrix arrangement of 3 rows by 3 columns. Color images capture different parts of the central eyespot and the peripheral region containing feather barbs. White feather barbs [Figs. 3(a)-3(c)] have a similar orientation to the adult iridescent peacock [Figs. 3(d)-3(f)]. Feather barbs in the young iridescent peacock have a different orientation [Figs. 3(g)-3(i)]. Different user-defined regions of interest of size 101 x 101 pixels (2.11 mm^2) were selected for further analysis. These are feather barb segments covered with many barbules.
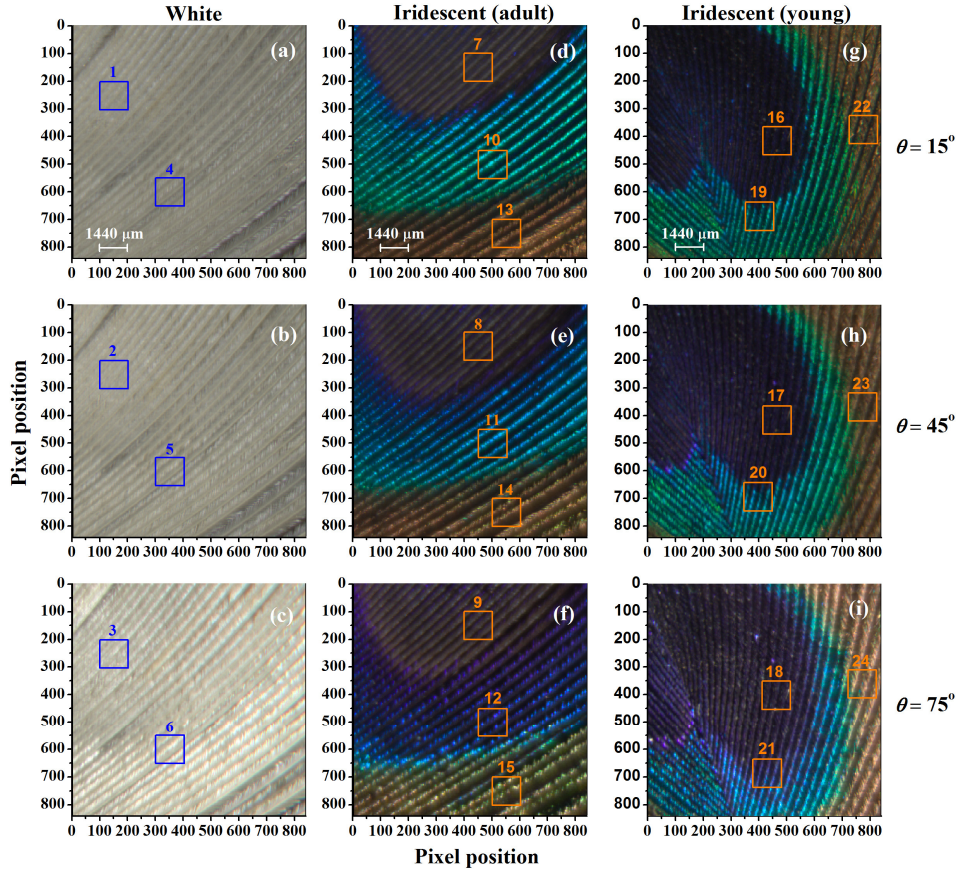
Fig. 3. Spatial color maps of peacock tail feathers. The entire selected imaging areas (size 841 x 841 pixels) as a function of the illumination angle θ. For each color image, at each pixel position the spectral reflectance function was mapped to CIE XYZ tristimulus values and then converted to the sRGB color space for visualization. Panels (a), (b), and (c) (left column), (d), (e), and (f) (central column) and (g), (h) and (i) correspond to the white peacock (*P. cristatus* mut. alba), the adult iridescent peacock (*P. cristatus*) and the young iridescent peacock (*P. cristatus*) at the illumination angle θ of 15 °, 45 ° and 75 °, respectively. Open squares (size 101 x 101 pixels) labeled from "1" to "24" indicate different user-defined regions of interest. Squares in the left column labeled as "1", "2", "3" and "4", "5" and "6" indicate a non-iridescent white area in the central eyespot and in the periphery of the eye region, respectively. Squares in the central column labeled as "7", "8", "9" and "10", "11", "12" and "13", "14", "15" indicate a blue iridescent area of the central eyespot and a green and a brown iridescent area in the periphery of the adult peacock feather, respectively. In the right column, squares labeled as "16", "17", "18" and "19", "20", "21" and "22", "23", "24" indicate a blue iridescent area of the central eyespot and a green and a brown iridescent area in the periphery of the young peacock feather, respectively.

3.2 Global spectral analysis

Figure 4 shows the mean spectral reflectance factor [44] of each selected area in Fig. 3. Each mean reflectance factor was obtained from the average of 101 x 101 = 10201 reflectances (i.e. the reflectance of each pixel). Reflectance values are grouped in 8 different panels in a matrix arrangement of 3 rows by 3 columns. The magnitude of the reflectance factor changes from place to place due in part to the spatial configuration and orientation of feather barbs. Reflectance spectra in the white peacock have never been analyzed before. White barbs exhibit non-iridescent effects [Figs. 1(e) and 1(f)] and mainly shift the reflectance factor in the vertical axis as a function of the illumination angle [Figs. 4(a) and 4(b)]. The results in the

white peacock indicate that shape of reflectance curves is very similar to that of the *Platalea regia* white feathers as measured with conventional spectrometers [60].
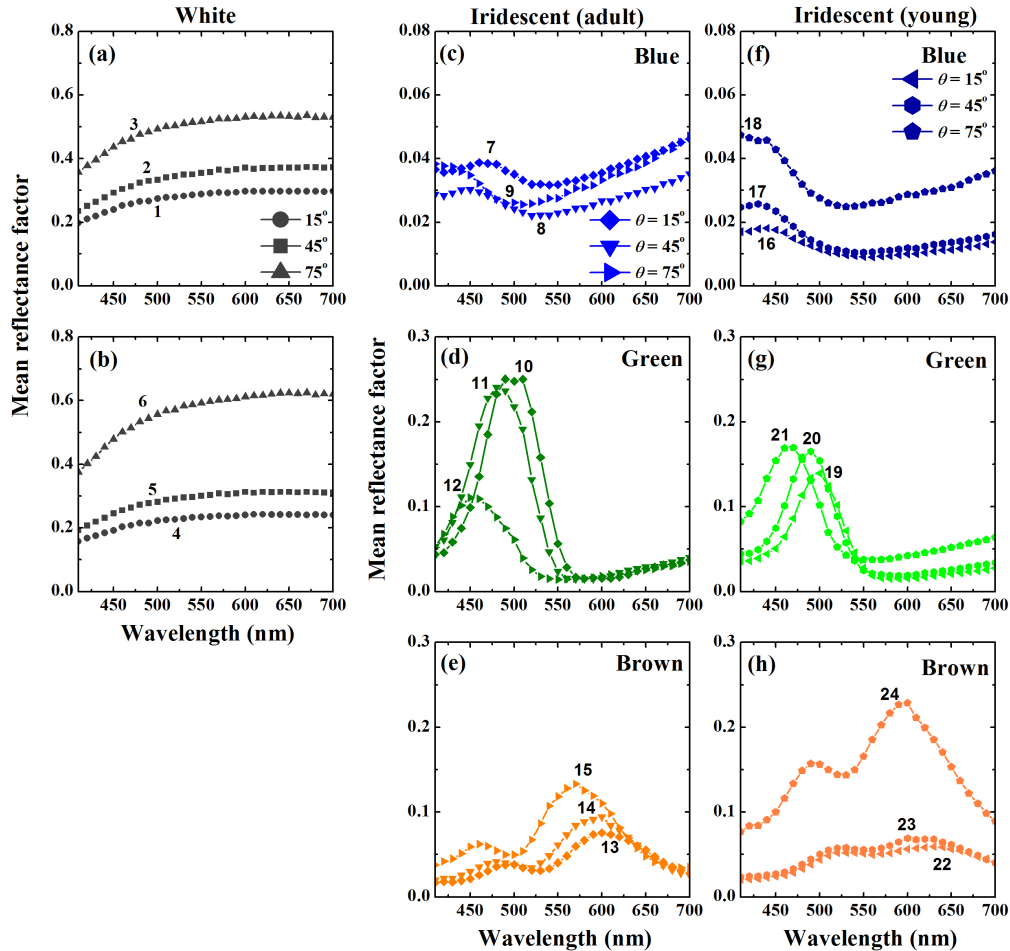

Fig. 4 . Mean reflectance factor of peacock tail feathers. Mean spectral reflectance factor as a function of the illumination angle. Panels (a) and (b), (left column), (c), (d) and (e) (central column) and (f), (g) and (h) correspond to a white peacock (*P. cristatus* mut. alba), an adult iridescent peacock (*P. cristatus*) and a young iridescent peacock (*P. cristatus*), respectively. Numbers in each curve labeled from "1" to "24" indicate the mean spectral reflectance factor of each selected region in Fig. 3. Each mean reflectance factor was obtained from the average of 10201 reflectances.

In general, the shape of the reflectance factor in iridescent feather barbs is similar to that measured with standard spectrometers [7–9]. The reflectance factor shifts to shorter wavelengths as the illumination angle *θ* changes from 15 ° to 75 °. Blue iridescent effects in the adult peacock are weak [Fig. 4(c)]. The spectral peaks from 460 nm to 410 nm are very similar to the value at 700 nm. This gives rise to the visual perception of magenta, due to the additive combination of blue and red reflected wavelengths. This red component of this effect may originate from melanin pigment [9]. In contrast in the young peacock feathers the spectral peaks from 440 nm to 410 nm are more intense than that at 700 nm [Fig. 4(f)]. In green iridescent feather barbs, the wavelengths at which each reflectance factor is a maximum were similar between the adult and the young peacock. The spectral reflectance maxima range from 490 nm to 450 nm in the adult and from 500 nm to 470 nm in the young peacock [Figs. 4(d) and 4(g)]. However, this is not the case in brown feather barbs and differences are higher

[Figs. 4(e) and 4(h)]. In the red part of the spectrum, the spectral maxima range from 600 nm to 570 nm in the adult and from 630 nm to 600 nm in the young peacock. In the blue part of the spectrum, the spectral maxima range from 500 nm to 460 nm in the adult and from 520 nm to 490 nm in the young peacock. These differences can be attributed to the existence of different sub-micron 2D photonic structures within the cortex of barbules [Figs. 1(b) and 1(d) and Table 1] [7, 8]. This issue will be discussed further later.

3.3 Analysis of eigenimages

PCA for the 10201 reflectances in each selected imaged surface of peacock feathers were performed (Fig. 3). Then, we examine the spectral variability within each imaged surface across each principal component direction separately. For each principal component, the scores $\boldsymbol{\alpha}_i$ in Eq. (1) provide the spatial distribution of pixels in the imaged surface and preserve the spectral information of the eigenvectors $\mathbf{S}_i$. Reconstruction of reflectance spectra along each principal component direction $\mathbf{R}'_k$ was performed by taking the mean reflectance factor $\overline{\mathbf{R}}$ and the corresponding eigenvector, $\mathbf{R}'_k = \overline{\mathbf{R}} + \boldsymbol{\alpha}_k \mathbf{S}_k$ [58]. Then, the resulting reflectance spectra can be displayed in sRGB color space producing characteristic spatial color patterns associated with each principal component direction or "eigenimages" [38, 39, 58]. For instance, Figs. 5(a) and 5(b) exemplify the original and the first three eingenimages of the green and brown iridescent feather barbules of the adult peacock at the illumination angle θ of 15° and 75°, respectively.
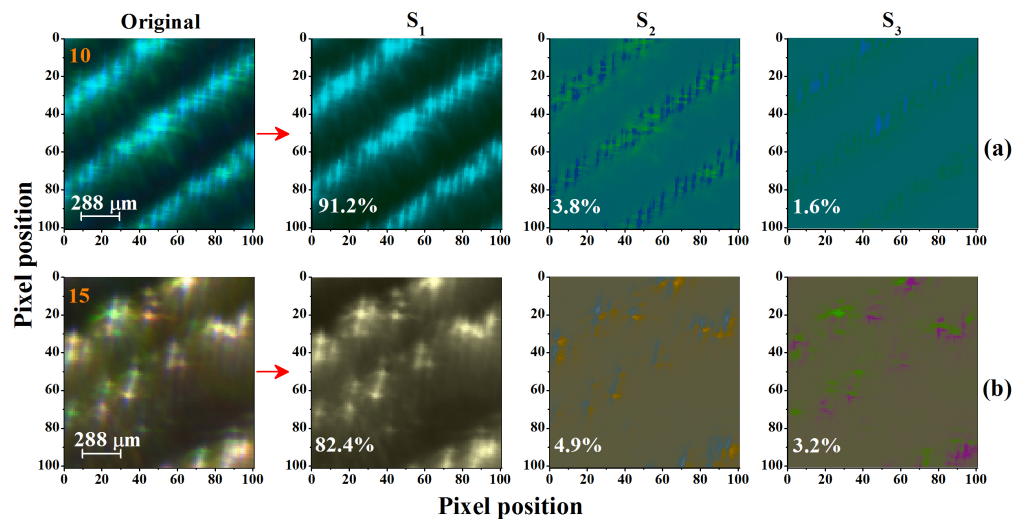

Fig. 5 . Example of eigenimages in the sRGB color space. The first row indicates the original imaged surface. Numbers in orange indicate the selected region annotated in Fig. 3. The subsequent rows indicate the reconstruction of reflectance spectra that result by the linear combination of the mean reflectance factor (Fig. 4) and the first three eigenvectors separately. Panels (a) and (b) show green and brown iridescent feather barbs of the adult peacock (*P. cristatus*) at the illumination angle θ of 15° and 75°, respectively. For each eigenimage, numbers in white indicate the percentage of variance explained by each associated eigenvector.

In general, the total spectral variability within each imaged surface is not very large. This is because each feather barb contains many identical barbules placed in a quasi-periodic spatial organization and each individual barbule has the same sub-micron 2D photonic structure inside [1, 9]. In each imaged surface the first eigenimage contains most of the spatial details and the corresponding eigenvector points to the weighted average direction (Eq. (1) [40]. In the examples provided in Figs. 5(a) and 5(b), the eigenvector indicates an overall cyan and yellow, respectively with spectral maxima located at 490 nm in green barbules and at 570 nm and 460 nm in brown barbules, respectively. The subsequent eigenimages represent

different corrections that are related to the random spatial displacements of barbules and their orientations. The first few eigenimages retain most of the total percentage of explained variability. In Figs. 5(a) and 5(b), 3 and 5 eigenvectors respectively, were necessary to account for more than 95% of total variance. The PCA data from these peacock feathers corroborate the existence of a few principal component directions that explain a large amount of variance and many principal component directions with negligible variance in a large number of reflectance data sets [32, 36–40, 58].

3.4 Principal component analysis similarity factors

PCASF values were calculated and contrasted. For instance, Fig. 6(a) shows the PCASF between brown and white feather barbs as reference. The standard PCASF and the WPCASF were calculated. The number of principal components k in Eqs. (2) and (3) was varied to account for at least 90%, 95% and 99% of total variance. At 90% of total variance, the number k was equal to 4, 5 and 3 at $\theta = 15°$, $45°$ and $75°$, respectively. At 95% it was equal to 9, 11 and 6 at $\theta = 15°$, $45°$ and $75°$, respectively and at 99%, k was equal to 24, 25 and 16 at $\theta = 15°$, $45°$ and $75°$, respectively. The results conclude that the PCASF depends on the number k and increases as the total percentage of explained variance increases. However, WPCASF is nearly independent of the total variance explained by the principal components. The standard PCASF approach weights all the principal components equally (Eq. (2) and the number of loading vectors with low variance is inappropriately high at 95% and 99% of total variance. These loading vectors are usually associated with different sources of noise from the multispectral imaging acquisition system [37–39, 58] and mask the comparison between the spatial reflectance patterns from feather barbs. Therefore, the WPCASF was chosen in subsequent analyses and it was calculated to account for at least 95% of total variance.
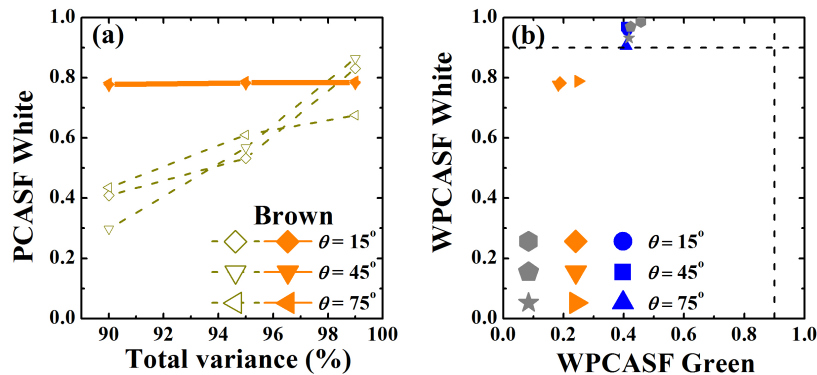

Fig. 6. PCA-based similarity factor in adult peacock feather barbs. (a) Example of PCASF between brown (*P. cristatus*) and white feather barbs as reference (*P. cristatus* mut. alba). The number of principal components varied to account at least 90%, 95% and 99% of total variance of reflectance spectra. Diamonds, down and left triangles indicate the PCASF at the illumination angle θ of 15 °, 45 ° and 75 °, respectively. Open symbols connected by dashed lines correspond to the standard PCASF. Solid symbols connected by solid lines correspond to the WPCASF. (b) WPCASF plots (95% of total variance) with the white and green iridescent feather barbs as reference. Grey, blue and orange symbols indicate the WPCASF of white non-iridescent, blue and brown iridescent feather barbs, respectively. Hexagons, diamonds and circles correspond with $\theta = 15$ °; pentagons, down triangles and squares with $\theta = 45$ ° and starts, up and right triangles with $\theta = 75$ °. Dashed lines indicate the tolerance limit at 0.9.

Figure 6(b) represents the WPCASF using two different spectral categories: white feather barbs at the centre of the white eyespot [Figs. 3(a)-3(c), squares "1", "2" and "3"] (labeled "WPCASF white") and green iridescent barbs [Figs. 3(d)-3(f) squares "10", "11" and "12"] (labeled "WPCASF green"). As a control condition, white feather barbs were compared between the centre of the eyespot and the peripheral part of the eye region [Figs. 3(a)-3(c), squares "4", "5" and "6"]. It was concluded that the WPCASF white was always higher than 0.9 at all illumination angles. We establish 0.9 as a tolerance limit in subsequent analyses.

Figure 6(b) clearly shows that iridescent brown and blue feather barbs are more similar to white barbs (WPCASF white > 0.7) than to iridescent green barbs (WPCASF green < 0.5). Further, blue iridescent barbs are spectrally similar to the white peacock (WPCASF white > 0.9). This is due to the location of the selected area in the adult peacock in the peripheral part of the eyespot where blue iridescence is weak [see Figs. 3(d)-3(f) squares "7", "8" and "9" and Fig. 4(c)]. Previous studies have established the chemical, structural and mechanical similarities between blue iridescent and white peacock tail feathers [45, 46]. Here we report their similarity from the spectral point of view. Figure 7 represents in a 3D space the WPCASF between the adult and young peacock feathers. Three different spectral categories were established: blue, green and brown taking the adult peacock as the reference sample [Figs. 3(d)-3(f)].
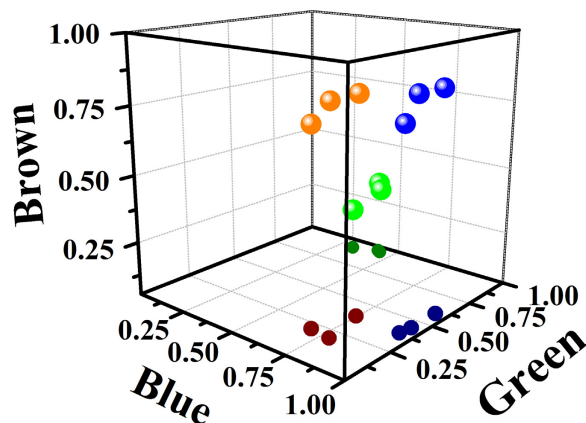

Fig. 7. PCA-based similarity factors in young peacock feather barbs. WPCASF (95% of total variance) with the blue, green and brown iridescent feather barbs from the adult peacock as reference. Spheres represent the WPCASF at different illuminant angles. Blue, green and brown spheres indicate the WPCASF of the blue, green and brown young iridescent feather barbs. Solid circles indicate the projection in the plane that corresponds with the blue and green WPCASF.

Blue and green iridescent barbs in the young peacock are similar to the blue and green counterparts in the adult at all illumination angles (WPCASF > 0.9). Comparisons between different iridescent feather barbs (e.g. adult blue versus young green etc.) always exhibit lower spectral similarity (WPCASF < 0.9). The spectral similarity was also lower than 0.9 in brown feather barbs (0.7 < WPCASF < 0.8). The influence of the area selected in the young peacock was also established by using a search procedure that maximizes the WPCASF within the brown region [Figs. 3(g)-3(i)]; in this instance WPCASF was always below 0.8.

4. Conclusion

Micro-scale structures of peacock feathers comprise complex branching patterns of barbs and barbules that depend on their surface curvature, twist, orientation distributions, etc., and change during feather growth [1, 6, 9, 10, 47, 48]. The spatial average over many barbules smoothes the reflectance spectra created by sub-micron 2D photonic crystal structures within the cortex surface of each single barbule and spread reflected light over a wide angular range [1, 9, 11]. Optical methods for investigating peacock feathers often provide single-point spectral data using conventional spectrometers that average over small feather patches with typical size of a few millimeters [1, 7–9, 12, 13]. This makes the research on the micro appearance of peacock tail feathers and texture analysis very difficult. Multispectral and hyperspectral imaging methods can offer advantages for characterization of surface materials by collecting both spectral and spatial information simultaneously [22, 58]. In this work we propose a multispectral imaging arrangement that has an excellent spatial and spectral performance in the visible part of the spectrum using commercially available optical

components. We measured components of the multispectral BRDF of feather barbs containing many barbules as a function of the illumination angle. We applied PCASF to classify their spatially-varying reflectance patterns. Spectral pattern matching was investigated in user-defined regions of interest within the eyespot region of the common peacock (*P. cristatus*) as well as in the white peacock (*P. cristatus* mut. alba). Each user-defined region of interest consisted of a small area of 2.11 mm^2 containing 10201 reflectances, i.e., one at each pixel of the imaged surface with a spatial resolution of 14.4 μm per pixel [58]. We demonstrate that the multispectral classification methodology based on PCA is an effective and useful non-destructive tool for spectral pattern recognition of iridescent feather barbs over spatially extended areas. WPCASF has successfully evaluated reflectance patterns by weighting a few key principal components that explain at least 95% of the total variance [32, 33, 35].

When iridescent effects are visually discernable in the feather samples used, we found a high degree of similarity within blue and within green iridescent barbules at different stages of feather development (Fig. 7, WPCASF> 0.9) [Figs. 1(a) and 1(c)]. Therefore, we conclude that these reflected light patterns are a good match across members of the same species. This also suggests that the different quasi-ordered organization of barbules can lead to the same smooth angle-dependent color variations during feather growth (Fig. 3). In addition, we found a spectral mismatch between the adult and young brown barbules (Fig. 7, WPCASF< 0.8). This is mainly due to the different sub-micron 2D photonic structures within the cortex surface of the young and adult feather barbules [Figs. 1(b) and 1(d), Table 1]. These spectral differences persist in the mean reflectance factor averaged over many barbules at different angular positions [Figs. 4(e) and 4(h)] and are comparable with the degree of similarity between feather barbules containing different photonic crystals (e.g. adult green versus young blue, etc.) (Fig. 7). Conversely, when iridescent effects are weak, we found a high degree of similarity between non-iridescent white and blue iridescence barbules [Fig. 6(b), WPCASF> 0.9]. This suggests that the 2D photonic structures inside each barbule in the adult peacock have a residual contribution to the peripheral region of the blue part of the eyespot (Fig. 3). Classification of these spatial reflectance patterns could be correlated with an effective color signaling process in peacocks [12].

The measurement of the multispectral BRDF in peacock feathers assumes that scattering occurs at each point source of the imaged surface separately and strong subsurface scattering from one spatial position to a different distant position is considered negligible [13]. It is also assumed that PCA operates in a static state and employs a linear transformation between the original reflectance spectra and a new set of uncorrelated loading vectors [30, 32, 35, 42]. Our findings conclude that the static linear assumption is entirely appropriate: PCA was performed in user-defined regions of interest under controlled conditions in the laboratory and is a successful linear model of reflectance spectra in peacock feathers. Our results also confirm that PCA provides a good description of a large number of surface reflectance data sets [36, 37, 40, 41, 58]. The WPCASF could be less efficient for the classification of spatial reflectance patterns in external dynamic situations under the influence of temporal disturbances such as in remote classification and bird migration for which other multivariate statistical classification methods [30, 37] might be more efficient. This issue deserves further investigation.

We have focused our analysis on the common peacock (*P. cristatus*) the feathers of which neither exhibit strong polarization effects in their reflectance spectra [7, 8] nor any UV reflectance maxima [12]. Classification of spatial reflectance patterns using PCA-based similarity factors can be applied to similar animal species when the effects of disorder and spatial averaging over repeated nanostructures contribute to smooth angular color variations [1, 9, 11]. However, there are iridescent birds and other animal species that have tetrachromatic vision, from the UV to the visible region, and show polarization effects and reflection maxima in the UV [1, 14–17, 19, 20, 43] and in the IR spectra [15, 22, 25]. This issue remains open and requires multispectral or hyperspectral polarization imaging methods in those spectral ranges [22, 25]. Here, combining a multispectral method in the visible spectrum and the WPCASF we describe an efficient classification method for the reflectance

properties of barbules that avoids current limitations associated with colorimetric analyses of bird colors [12, 17, 20, 43]. We suggest this multispectral classification method could be used effectively to elucidate novel perspectives in animal biometrics and the diagnosis of local spatial defects such as partial leucism.

Acknowledgments